Journal of Visualization, Vol. 9, No. 1 (2006)83-90

Flow on Blades of Wells Turbine for Wave Power Generation

Suzuki, M.*[1] and Arakawa, C.*[2]

*1 Department of Mechanical Engineering, Graduate School of Engineering, The University of Tokyo, 7-3-1 Hongo, Bunkyo-ku, Tokyo, 113-8656, Japan. E-mail: wells@cfdl.t.u-tokyo.ac.jp
*2 Interfaculty Initiative in Information Studies Graduate School of The University of Tokyo, 7-3-1 Hongo, Bunkyo-ku, Tokyo, 113-8656, Japan.

Received 14 January 2005
Revised 7 June 2005

Abstract : Wells turbine has the cascade whose stagger angle is 90°, namely the blades are perpendicular to the axial velocity. Good performance is required from 0° to 90° angle of attack because the turbine is operated in the oscillating airflow produced with wave energy. Furthermore, very interesting and complex flows are experimentally observed by the oil film method for large angles of attack where the performance is strongly influenced, especially, the self-starting. This paper tries to analyze the mechanism of these three-dimensional flows around the turbine with the flow visualization and the numerical analysis, focusing on the off-design condition.

Keywords : Flow visualization, Oil Film Method, Wells Turbine, Flow on Blades, Wave Power Generation.

1. Introduction

A wave-power-generating system of Oscillating Water Column (OWC) type is composed of a turbine-generator and an air chamber in which OWC converts wave energy into oscillating airflow. The wave energy is absorbed by the air chamber fixed or floating at the sea surface. A Wells turbine is used for the air turbine because it is suitable for the operation in oscillating airflow. The basic feature of the Wells turbine is that even though the cyclic airflow produces oscillating axial forces on the airfoil blades, the tangential force on the rotor is always in the same direction. This induces the rotation of the rotor and produces a power output without the need for the sophisticated rectifying valves. The turbine rotor consists of several symmetric airfoil blades arranged around a central hub, and the stagger angle is 90 degrees. These characteristics simplify construction of OWC type wave energy converters. The characteristics became clear by the performance tests, which were done in the wind tunnel (Raghunathan, 1995; Suzuki et al., 2000). The 3-D Navier-Stokes equations were solved numerically to predict the characteristics of a Wells turbine with computational fluid dynamics (CFD) codes including commercial ones (Watterson et al., 1997). But they did not cover the stall condition and detailed simulation of the performance.

In order to understand the flow field, the authors visualize it by using an oil film method in the water tunnel and an in house CFD code. This research aims to analyze the mechanism of the 3-D flows around the turbine with the flow visualization.

2. Experimental Apparatus

2.1 Performance Test

Figure 1 is a schematic view of the experimental apparatus. The inside diameter of the casing $D_c = 2R_c$ is 304.4 mm, and the hub diameter $D_h = 2R_h$ is 215 mm. Figure 2 describes the rotor profile, which has 8 blades, a chord length of 73.5 mm, a NACA0021 wing section, a solidity of 0.7 at the root mean square of the radius, $R_{RMS} = \sqrt{(R_c^2 + R_h^2)/2}$, and a tip clearance of 1.0 mm. The wind tunnel is of suction type. The measured data are the pressure drop across the turbine, the turbine torque, the rotational speed and the flow rate. The Reynolds number is described with the representative velocity and length, which are assigned the relative velocity at the tip, $\sqrt{U^2 + V_a^2}$, and the blade's chord length, respectively. The Reynolds number is fixed at about 1.7×10^5 when the angle of attack is less than $14.5°$, and approximately $0.42\times10^5\sqrt{1+1/\tan^2\alpha}$ when it is larger than $14.5°$. U, V_a and α are the blade speed of the tip, the axial velocity and the angle of attack, respectively.

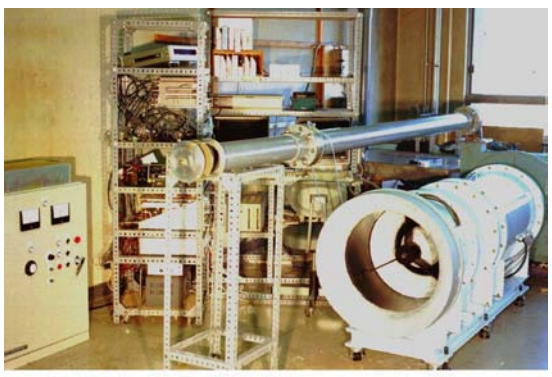

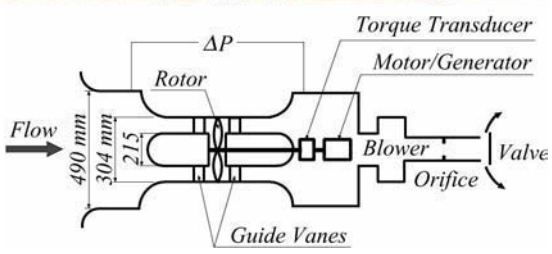

Fig. 1. Schematic explanation of experimental apparatus for the performance test.

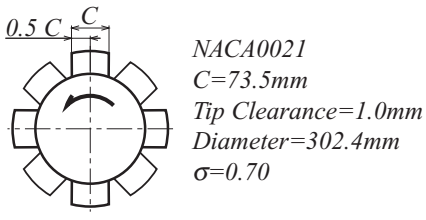

Fig. 2. Profile of rotor.

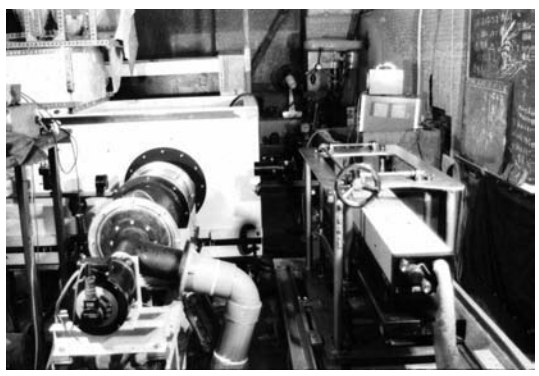

Fig. 3 Experimental apparatus for flow visualization.

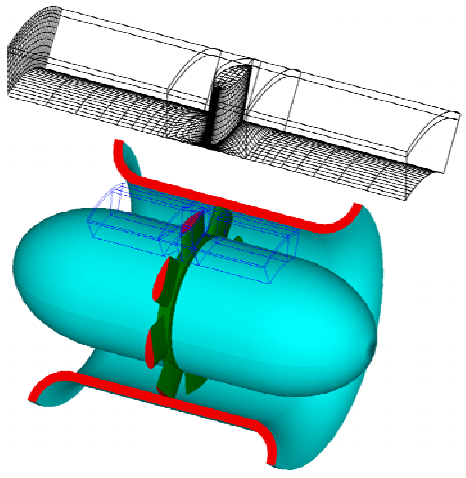

Fig. 4. Grid system of domain decomposition around Wells turbine.

2.2 Flow Visualization

Figure 3 is an overall view of circulating-water tunnel in which the flow around the Wells turbine can be visualized with flow visualization techniques. The size of this apparatus and the Reynolds number are the same as for the wind tunnel in the above performance test. The flow visualization technique used in this water tunnel is the oil-film method. The test section is covered with the transparent acrylic casing so that the inner flow can be observed. The pump pushes the water from the upstream tank through the turbine, the orifice and the flow control valve, and it discharges to the upstream tank.

The oil film method uses Titanium dioxide, Liquid paraffin and Oleic acid which is mixed with a ratio of 10:5:6 by weight. The rotational speed is 200 rpm when the angle of attack is less than $14.5°$, while the axial velocity is approximately 0.8 m/sec when the angle of attack is larger than $14.5°$. The Reynolds numbers are 1.7×10^5 at $\alpha=0°$, 1.6×10^5 at $\alpha=15°$, 1.2×10^5 at $\alpha=19°$.

3. Numerical Method

The numerical method in this research uses the grid system of domain decomposition. The authors developed the CFD code in order to understand complex flows such as turbomachinery. The incompressible and steady Navier-Stokes equations are solved with the SIMPLE (Patankar, 1980) algorism for a pressure-correction, and the collocated grid (Rhie and Chow, 1983) for a general curvilinear coordinate system. The code was validated on 2D airfoils. It was shown that the calculation results agreed with experimental results below the stall angle for Reynolds numbers over 10^6 (Suzuki et al., 2002). The calculation results agreed with experimental results even on a very coarse grid, 76x51 (Suzuki and Arakawa, 2003).

Figure 4 shows the grid system of domain decomposition around the Wells turbine. The calculated domain is extended to 1-radius length in the upstream direction and 3-radius lengths in the downstream direction from the blade annulus. As periodic boundary conditions are assumed in the circumferential direction, only one blade-to-blade passage, that is, a 1/8 region is required for the simulation of the machine. The calculated domain is divided into 24 blocks including the 4 blocks in the tip clearance. The mesh around the blade surface consists of 140 points along the surface of the airfoil, 30 points along the wake in the C-figure configuration, and 39 points in the spanwise direction. 5 points are used in the tip clearance. The total number of grids is about 320,000 nodes.

The boundary conditions are specified for the velocity at the inlet. As for the outlet, the velocity is calculated by the Neumann condition and the axial velocity is corrected to be the same as the inlet flow rate afterwards. The surfaces of blade, hub, casing and blade tip are treated with no-slip conditions. The static pressure at the boundary is assumed to be the Neumann condition, except between the domains. The boundary values between domains are extrapolated and averaged with each other.

4. Experimental Results and Discussion

4.1 Performance of Turbine

Figures 5 ~ 7 show the results of the performance test and the numerical calculations for the Wells turbine. The nondimensional factors used in the experimental investigation are explained in the following. Flow coefficient, ϕ, angle of attack, α, torque coefficient, C_T, pressure drop coefficient, ψ, and efficiency, η, are defined as:

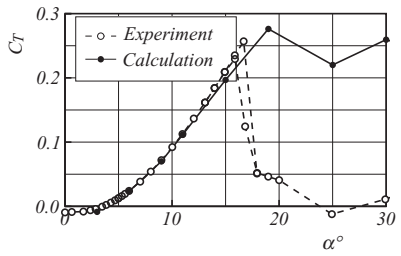

Fig. 5. Torque coefficient.

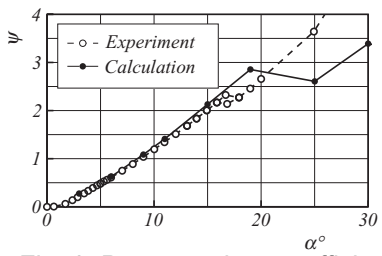

Fig. 6. Pressure drop coefficient.

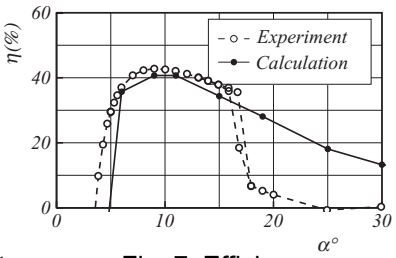

Fig. 7. Efficiency.

$$\phi = \frac{V_a}{U} = \tan\alpha, \quad C_T = \frac{T}{\frac{1}{2}\rho(U^2 + V_a{}^2)AR_t}, \quad \psi = \frac{\Delta P}{\frac{1}{2}\rho(U^2 + V_a{}^2)}, \quad \eta = \frac{C_T}{\psi\phi} \tag{1}$$

where the nomenclatures are U=blade speed of the tip, V_a = axial velocity, T = torque, ΔP = pressure drop across the blade, R_t = radius of the rotor, R_h = radius of the hub, annulus section area of $A = \pi(R_t^2 - R_h^2)$, and ρ = air density. The Wells turbine operated with constant rotational speed has the unique characteristics that the torque is proportional to the square of the flow rate, and the pressure drop is proportional to the flow rate in the operation before stall.

Figures 5 ~ 7 show the torque coefficient, the pressure drop coefficient and the efficiency of the Wells turbine, respectively. Wells turbines start to rotate from an attack angle of 90°. As the rotational speed increases, the angle of attack and the torque decrease. The turbine reaches the condition before the stall point where the torque achieves minimum value (25° in Fig. 5). Since this torque in badly designed turbines is negative, the turbine usually cannot accelerate by itself to a higher rotational speed. However, the turbine can overcome the negative torque region and arrive at the standard operation with the inertia forces of the turbine and the motor. The turbine is automatically driven into the standard operating range where a large torque is produced if the angle of attack is moderate, such as 10°. The swell of wave motion provides a good opportunity to move the preliminary operating condition of large attack angle to the standard operating condition when the swell changes from a big wave to a small wave. When this happens the inertia of the turbine and the generator play an important role in keeping the rotational speed. At this moment the angle of attack changes from a large angle of attack in the stall condition to a small angle in the standard operating range. Thus, the characteristics in the stall condition are also very important in order for the Wells turbine to achieve total performance.

In Figures 5 ~ 7, the numerical predictions for the standard operating condition up to the stall angle (about 16°) coincide with the experimental data. The stall is predicted at an angle of attack of about 25°, although it does not correspond with the experimental data. Thus, it will be possible to investigate the stall mechanism using the simulated result. It is hoped that in the future the performance will be predicted in more detail and improved with the simulation.

4.2 Flows around the Blades

Figure 8 shows the flow patterns on the Wells turbine visualized with the oil-film method. Figure 8(a) shows the flow on the pressure surface when the angle of attack is $\alpha = 0°$. Figure 8(b) shows the flow on the suction surface whose angle of attack is $\alpha = 11°$, Fig. 8(c) shows the flow on the suction surface whose angle of attack is $\alpha = 15°$ just before the stall, and Fig. 8(d) shows the flow on the suction surface whose angle of attack is $\alpha = 19°$ after the stall. Figure 9 shows the surface streamlines predicted with numerical calculation corresponding to Fig. 8. The flow patterns in Figs. 8 and 9 look very similar to each other.

In Fig. 8(a) the oil streaks on the pressure sides form a pattern similar to a logarithmic spiral because of the centrifugal force. The figures for the other angles of attack show the same patterns. In Figs. 8(b) and 8(c), the pattern on the suction sides show that the fluid near the blade surface flows in the circumferential direction, and the separation region (1) on the blade is observed near the trailing edge. What is most important in this oil pattern is the reverse flow (2), which initiate at the corner of

the trailing edge and tip. This phenomenon manifests with a kind of an envelope line of oil streaks flowing in the upstream direction. It is supposed that this reverse flow (2) shown with oil streaks triggers off to induce a large scale separation, which creates the counterclockwise swirl (5) shown in Fig. 8(d). Although Fig. 9(b) overestimates the reverse flow (2) due to the separation, the flow patterns in Fig. 9 can show overall characteristics of the flow in Fig. 8 of oil-film experiments.

(a) $\alpha = 0°$

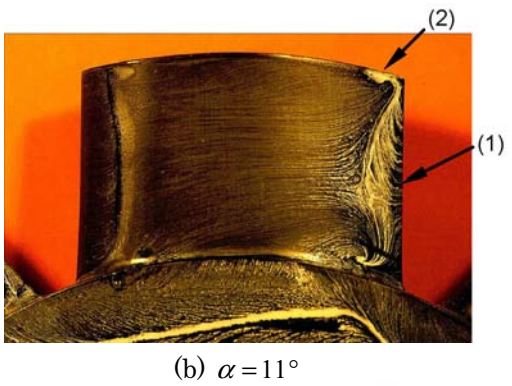

(b) $\alpha = 11°$

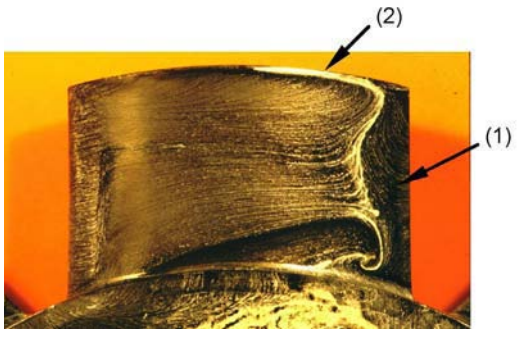

(c) $\alpha = 15°$

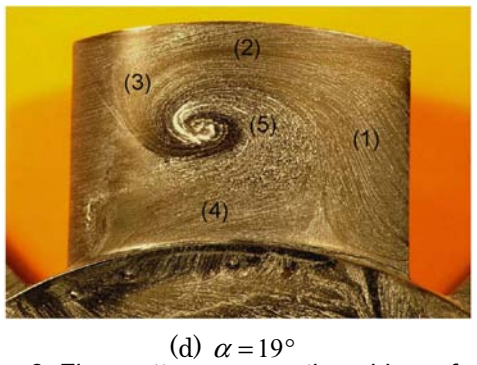

(d) $\alpha = 19°$

Fig. 8. Flow patterns on suction-side surface with oil film method.

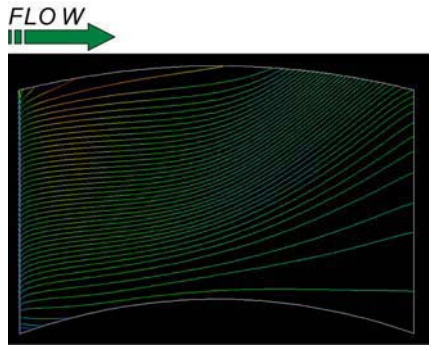

(a) $\alpha = 0°$

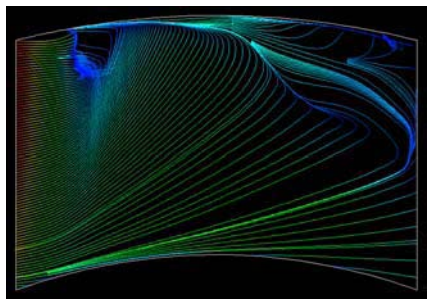

(b) $\alpha = 15°$

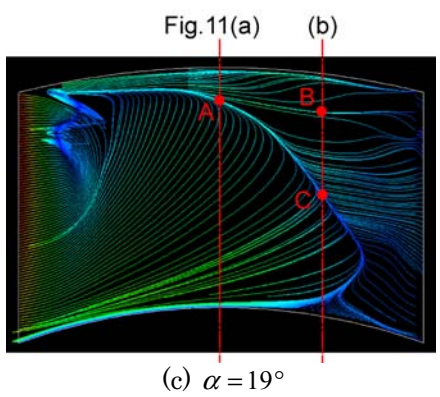

(c) $\alpha = 19°$

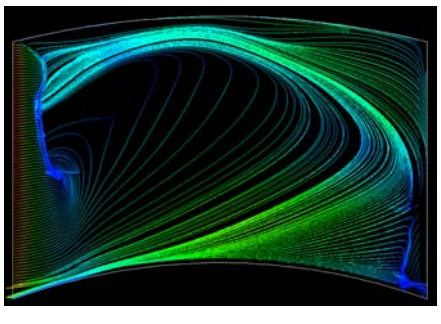

(d) $\alpha = 30°$

Fig. 9. Flow patterns on suction-side surface in calculation.

Figure 9(d) is added to show the calculated flow that completely stalls at $\alpha = 30°$, because Fig. 9(c) does not completely stall at $\alpha = 19°$. Figure 9(d) shows a similar large counterclockwise swirl to the experimental flow in Fig. 8(d). Using streamlines flowing from the lines of leading edge, Fig. 10 exhibits the swirl which is created on the blade surface and goes down in the stream. Figure 10 shows the vortex flow at $\alpha = 19°$ corresponding to Fig. 9(c), whose swirl is a large and strong vortex produced near the leading edge.

The authors have been very interested in the existence of the swirl, which has a clear eye in

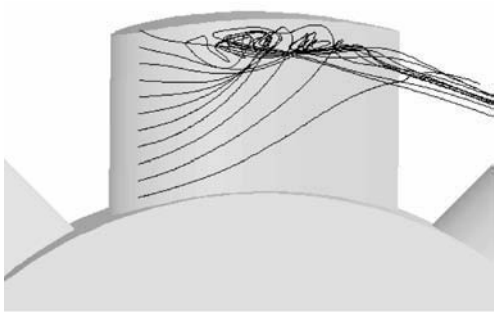

Fig. 10. Vortex flow created on blade going downstream $\alpha = 19°$.

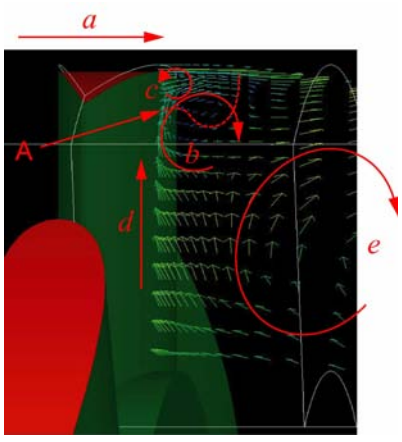

(a) $x/l = 0.5$

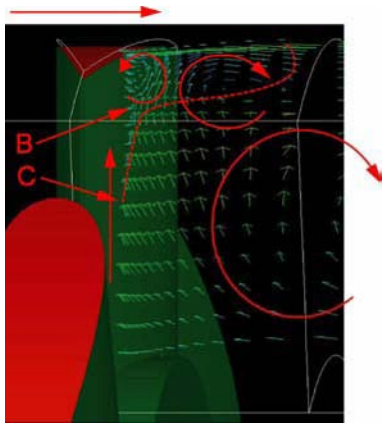

(b) $x/l = 0.75$

Fig. 11. Velocity vectors in cross-section at $x/l = 0.5$ and $x/l = 0.75$ where 3 longitudinal vortices appear on suction side at $\alpha = 19°$ with numerical analysis.

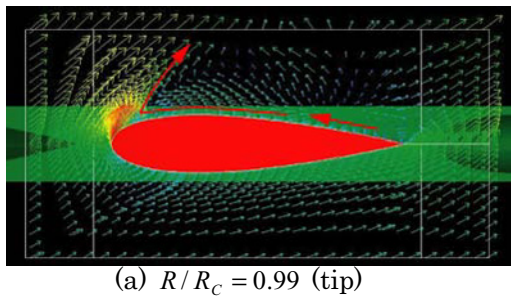

(a) $R/R_C = 0.99$ (tip)

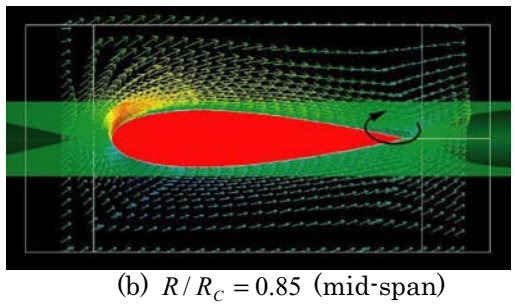

(b) $R/R_C = 0.85$ (mid-span)

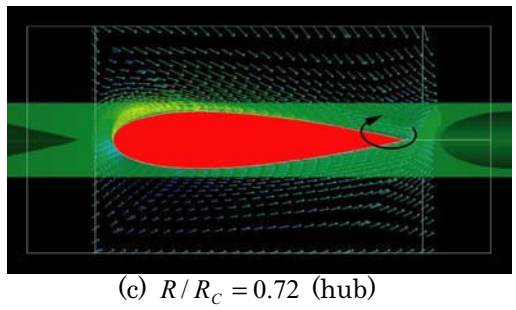

(c) $R/R_C = 0.72$ (hub)

Fig. 12. Velocity vectors around blade at $\alpha = 19°$ degrees in numerical analysis.

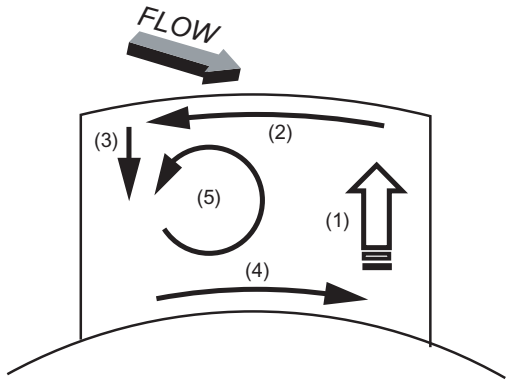

Fig. 13. Creation mechanism of stall in Wells turbine.

the oil-film pattern on the blade, and the reason for the flow patterns in the stall curling in the counterclockwise direction. The understanding and clarification of the creation mechanism of the swirl will be useful for improving the characteristics of the performance of Wells turbines. The calculated results are investigated in detail in order to understand the physical phenomena described below.

5. Creation Mechanism

Figure 11 shows the velocity vectors in the cross-section perpendicular to the rotor in Fig. 9(c) where 3 longitudinal vortexes appear on the suction side. The clockwise vortex *b* of middle size near the tip of the blade is a so-called tip vortex, produced with leak flows *a* from the tip clearance. The counterclockwise vortex *c* of small size in the corner between the tip vortex and the blade is the secondary vortex produced by the tip vortex, and another large and clockwise vortex *e* is produced by the centrifugal forces *d* on the blade. The secondary vortex clearly appears at the location near the chord length $x/l = 0.5$, where x is the length from the leading edge, and l is the chord length. As the vortex is going down to the trailing edge, it becomes larger, as shown in the figure of $x/l = 0.75$. The tip vortex is going away from the blade as it is going down to the trailing edge. The flow *d* near the blade is moving from the hub to the tip because of the centrifugal forces in the boundary layer, and the fluid of low speed accumulates at the tip region on the suction side. Hence the separation first appears at the tip because the tip vortex, the secondary vortex and the centrifugal forces on the blade thicken the boundary layer at the tip. The reverse flow from the trailing edge to the leading edge appears above a dashed line, which is drawn from a position A, and a position C in Figs. 11(a), 11(b) and 9(c). The position A and B show the location where the separation by the secondary vortex occurs. The position C shows the location of the separation initiated at the trailing edge.

Figure 12 plots velocity vectors around the rotor in 3 cross-sections of circumferential directions. In Fig. 12(a) near the tip $R/R_c = 0.99$, where R_c is the radius of the casing, the boundary layer becomes thick on the suction side of the airfoil, and the reverse flow occurs even at the chordwise position of 20% as the flow is unable to stand up against the adverse pressure gradient from the leading edge to the trailing edge. The low speed flow in the boundary layer on the blade is concentrated at the tip by the centrifugal forces, the tip vortex and the secondary vortex. In Figs. 12(b) and 12(c) the flows from mid-span, $R/R_c = 0.85$, up to the hub, $R/R_c = 0.72$, produce a reverse flow only at the trailing edge. The flows in the boundary layer near the hub at the suction surface are going away from the leading edge to the trailing edge because the boundary layer becomes so thin that it is difficult to separate at the leading edge. This behavior is produced by both the suctional effect of the centrifugal force and supplement of the flow from the downstream to the hub.

Figure 13 illustrates the mechanism of 3-D stall creation observed on the suction side based on the understanding described above. The flow is produced in turn from (1) to (4), and the counterclockwise vortex (5) is created.

(1) The radial flow is produced by the centrifugal force in the separation region, which appears near the trailing edge in Figs. 8(b) and 8(c).

(2) The reverse flow occurs at the tip because it is unable to stand up to the adverse pressure gradient as the boundary layer becomes thick in Fig. 12(a).

(3) The flows near leading edge go down from the tip to the hub on the separation line in Fig. 9(d) because the pressure at the hub is lower than at the tip, as the flows near the hub are not separated.

(4) On the other hand, the flows near the hub go from the leading edge to the trailing edge because the separation does not occur at the leading edge in Figs. 12(b) and 12(c).

(5) It is found that the above 4 flows result in producing the counterclockwise vortex on the blade when the turbine stalls.

6. Conclusion

The Wells turbine produces a complicated flow field due to the peculiar arrangement of blades, which can rotate in the same direction irrespective of the oscillating airflow. In order to understand these flows, flow visualization is carried out with an oil-film method in the water tunnel. Very interesting and complex flow patterns are observed especially in the flow of large angle of attack.

The authors developed a CFD code in order to understand these phenomena in detail. The complex flow for the stall condition such as a large angle of attack is also well simulated, and strong vortices can be observed.

A strong counterclockwise vortex appears on the suction surface in the stall condition. The main reason that the vortex is counterclockwise is found to be that the separation, as a trigger of vortex, occurs in the forward position of the chord at the tip in the suction surface where the fluid of low speed gathers due to the suction effect of the boundary layer on the rotating blade and the tip vortex.

References

Patankar, S. V., Numerical heat transfer and fluid flow, (1980), McGraw-Hill, New York.
Raghunathan, S., The Wells Air Turbine for Wave Energy Conversion, Prog. Aerospace Sci., 31 (1995), 335-386.
Rhie, C. M. and Chow, W. L., Numerical Study of the Turbulent Flow Past on Airfoil with Trailing Edge Separation, AIAA J, 21-11 (1983), 1525-1532.
Suzuki, M. and Arakawa, C., Guide Vanes Effect of Wells Turbine for Wave Power Generator, Int J Offshore and Polar Eng, ISOPE, 10-2 (2000), 153-159.
Suzuki, M., Fleig, O. and Arakawa, C., Comparison of Suitability of Different CFD Codes for Wind Turbine Blades, Proc of 5th JSME-KSME Fluids Eng Conf (Nagoya, Japan), JSME, (2002), 1359-1364, CD-ROM.
Suzuki, M. and Arakawa, C., Investigation of Calculation Accuracy and Domain Size around Isolate Airfoil, Proc 17th Symposium Computational Fluid Dynamics, JSFM, D1-6 (2003), CD-ROM, (in Japanese).
Watterson, J. K. and Raghunathan, S., Computed Effects of Tip Clearance on Wells Turbine Performance, 35th Aerospace Sci Mtg and Exh (Reno, NV), AIAA Paper, 97-0994 (1997).

Author Profile

Masami Suzuki: He received his BEng in Mechanical Engineering in 1976 from Tokyo Denki University. He also received his D.Eng. in Mechanical Engineering in 2002 from the University of Tokyo. He worked in Department of Mechanical Engineering, the University of Tokyo as a technical researcher in 1972. He works in Department of Mechanical Engineering, the University of Tokyo as a research associate since 1984. His research interests are Wave Energy Converting System, Computational Fluid Dynamics and Turbomachnery.

Chuichi Arakawa: He received his MEng in Mechanical Engineering in 1976 from the University of Tokyo. He also received his D.Eng. in Mechanical Engineering in 1980 from the University of Tokyo. He worked in Department of Mechanical Engineering, the University of Tokyo as a Lecturer in 1980, as an associate professor in 1981, and a professor since 1996. He worked in the University of Karlsruhe as a researcher in 1985-1986. His research interests are Computational Fluid Dynamics, Wind Turbine, and Energy Economics Simulation.